

Wavelet-based adaptive simulations of three-dimensional flow past a square cylinder

Giuliano De Stefano¹ and Oleg V. Vasilyev^{2,†}

¹Dipartimento di Ingegneria Industriale e dell'Informazione, Seconda Università di Napoli,
I 81031 Aversa, Italy

²Department of Mechanical Engineering, University of Colorado, Boulder, CO 80309, USA

(Received 3 September 2013; revised 21 March 2014; accepted 3 April 2014)

The wavelet-based eddy capturing approach is extended to three-dimensional bluff body flows, where the flow geometry is enforced through Brinkman volume penalization. The wavelet-collocation/volume-penalization combined method is applied to the simulation of vortex shedding flow behind an isolated stationary prism with square cross-section. Wavelet-based direct numerical simulation is conducted at low supercritical Reynolds number, where the wake develops fundamental three-dimensional flow structures, while wavelet-based adaptive large-eddy simulation supplied with the one-equation localized dynamic kinetic-energy-based model is performed at moderately high Reynolds number. The present results are in general agreement with experimental findings and numerical solutions provided by classical non-adaptive methods. This study demonstrates that the proposed hybrid methodology for modelling bluff body flows is feasible, accurate and efficient.

Key words: computational methods, flow–structure interactions, turbulence simulation

1. Introduction

The numerical simulation of unsteady vortex shedding flow past bluff bodies immersed in a fluid stream is of great importance in several scientific and technological areas. In particular, the prediction of the unsteady forces arising from fluid–structure interaction is a challenging issue for a number of fundamental engineering applications.

Even for two-dimensional bodies and two-dimensional flow configurations, the transition from two- to three-dimensional flow occurs at low Reynolds number and, most notably, the wake-induced forces are highly dependent on the development of flow structures arising at the onset of the transition (Sheard, Fitzgerald & Ryan 2009). The stability of the two-dimensional wake of cylinders with square cross-section has been the subject of extensive theoretical, experimental and numerical studies, e.g. Okajima (1982), Robichaux, Balachandar & Vanka (1999), Sohankar, Norberg & Davidson (1999), Saha, Muralidhar & Biswas (2000) and Luo, Chew & Ng (2003). It is generally agreed that the square cylinder wake is unstable to two main spanwise three-dimensional disturbances, which are referred to as ‘mode A’ and ‘mode B’ in

† Email address for correspondence: oleg.vasilyev@colorado.edu

the literature, similarly to what occurs for circular cylinders (Williamson 1996). The wavelengths of these spanwise-periodic three-dimensional structures are about 5.2 and 1.2 cross-sectional lengths, respectively (Robichaux *et al.* 1999; Luo *et al.* 2003). For the long-wavelength mode A, the critical Reynolds number (Re) has been observed to be around 160, while the short-wavelength mode B has been found to become unstable for $Re \approx 190$.

In order to numerically predict the essential features of the transitional shedding flow past a square cylinder, the extent of the computational domain in the homogeneous spanwise direction, where periodic boundary conditions are applied, must be sufficiently large to capture the evolution of the abovementioned three-dimensional disturbances. In addition, the numerical grid must be properly refined both close to the body surface, to resolve the kinematic boundary layer, and behind the obstacle, to simulate the wake flow accurately. Thus, direct simulation of unsteady flow past a square cylinder has a very high computational cost, even at low supercritical Reynolds numbers. Furthermore, the square cylinder flow is inherently a multiscale problem, where different fluid dynamics phenomena coexist. The shear layers separating from the edges of the cylinder share features with mixing layers, recirculating flows and separated boundary layers, as thoroughly examined by Lyn & Rodi (1994).

The natural ability of wavelet multiresolution analysis to identify and track energy-containing motions offers a unique framework for numerical simulations of bluff body flows. By decomposing the velocity field in terms of wavelet basis functions and retaining only significant wavelets, the degrees of freedom of the numerical solution and, thus, the associated computational cost can be drastically reduced with respect to non-adaptive methods (Vasilyev & Bowman 2000). The actual importance of the unresolved velocity field is controlled by the wavelet thresholding level that is assumed. For very low thresholds, the residual background flow can be completely neglected, resulting in the wavelet-based direct numerical simulation (WDNS) method, e.g. Schneider & Vasilyev (2010). On the other hand, the use of higher thresholding levels necessitates the introduction of a subgrid-scale (SGS) model that mimics the effect of the unknown residual motions, leading to the wavelet-based adaptive large-eddy simulation (LES) methodology, e.g. Goldstein & Vasilyev (2004) and De Stefano & Vasilyev (2010). The two different approaches use the same high-order adaptive wavelet collocation (AWC) method (Vasilyev & Bowman 2000; Vasilyev 2003) to resolve and ‘capture’ energy containing/dynamically important eddies on a near-optimal computational grid that automatically adapts to the solution in both position and scale. Due to this commonality, WDNS and wavelet-based adaptive LES are both referred to as eddy capturing approaches (De Stefano & Vasilyev 2012). With this methodology, due to the built-in wavelet-based grid adaptation, the spatially non-uniform meshing is not prescribed *a priori*, but is determined dynamically according to the time evolution of the flow field. The mesh is automatically refined where high gradients exist in the solution, thus ensuring adequate resolution of the important flow structures.

The main aim of the present study is to extend the wavelet-based eddy capturing approach to three-dimensional wall-bounded flows. The extended methodology is demonstrated for vortex shedding flow behind an isolated stationary prism with square cross-section. The presence of the cylinder is mimicked by using the Brinkman volume-penalization method, which results in a slight modification of the governing equations by adding an appropriate forcing term (Angot, Bruneau & Fabrie 1999). Differently from similar recent studies that make use of this approach in two

spatial dimensions, e.g. Keetels *et al.* (2007), in this work the volume-penalization methodology is applied to numerical simulations of three-dimensional flow around a two-dimensional obstacle. Furthermore, the hybrid wavelet-collocation/volume-penalization method for fluid–structure interaction (Kevlahan & Vasilyev 2005) is extended to adaptive LES of wall-bounded turbulent flows.

The rest of the paper is organized as follows. In §2, the combined volume-penalization/eddy capturing approach for the solution of incompressible bluff body flows is described. After introducing the square cylinder flow configuration in §3, the numerical experiments for WDNS and adaptive LES are presented and discussed in §4. Finally, some concluding remarks are made in §5.

2. Methodology

For the sake of clarity, the volume-penalization/eddy capturing hybrid method is discussed for the flow past a single two-dimensional bluff body, which is the subject of the present study. However, the numerical procedure can be easily generalized to the case of bodies with complex three-dimensional shapes and/or a set of obstacles.

2.1. The volume-penalized governing equations

The incompressible flow around the obstacle is governed by the following continuity and momentum equations

$$\frac{\partial u_i}{\partial x_i} = 0, \quad (2.1)$$

$$\frac{\partial u_i}{\partial t} + (u_j + U_j) \frac{\partial u_i}{\partial x_j} = -\frac{\partial P}{\partial x_i} + \nu \frac{\partial^2 u_i}{\partial x_j \partial x_j}, \quad (2.2)$$

where $P = p/\rho$ stands for the kinematic pressure, with ρ being the constant density of the fluid. The imposed uniform velocity field U_j corresponds to the free stream velocity, which is given and known. The fluid occupies the complement Ω_f , in the computational domain Ω , of the physical domain filled by the solid obstacle, Ω_s . The unknown perturbation velocity u_i must obey the following boundary condition on the surface of the obstacle:

$$u_i + U_i = 0 \quad \text{on } \partial\Omega_s, \quad (2.3)$$

which represents the no-slip condition for the total velocity field, along with appropriate boundary conditions on $\partial\Omega$.

According to the Brinkman volume-penalization approach (Angot *et al.* 1999), instead of solving the original equations (2.1) and (2.2) in the fluid domain Ω_f , with the associated boundary condition (2.3) on the body surface, the following penalized equations for the new unknown \tilde{u}_i are solved in the entire domain Ω :

$$\frac{\partial \tilde{u}_i}{\partial x_i} = 0, \quad (2.4)$$

$$\frac{\partial \tilde{u}_i}{\partial t} + (\tilde{u}_j + U_j) \frac{\partial \tilde{u}_i}{\partial x_j} = -\frac{\partial \tilde{P}}{\partial x_i} + \nu \frac{\partial^2 \tilde{u}_i}{\partial x_j \partial x_j} - \frac{\chi_s}{\eta} (\tilde{u}_i + U_i). \quad (2.5)$$

The additional term on the right-hand side of the penalized momentum equation (2.5) mimics the presence of a porous obstacle, where χ_s stands for the characteristic

(or mask) function associated with the obstacle domain. For a stationary body, the following definition holds

$$\chi_s(\mathbf{x}, t) = \begin{cases} 1, & \text{if } \mathbf{x} \in \Omega_s, \forall t, \\ 0, & \text{otherwise,} \end{cases} \quad (2.6)$$

so that, in practice, the original equations for the fluid region and the penalized equations for the porous obstacle are solved simultaneously. It should be noted that the penalized perturbation velocity \tilde{u}_i must satisfy the same boundary conditions on $\partial\Omega$, which are valid for the original field u_i .

The positive constant η , which has the dimension of time and reflects the fictitious porosity of the obstacle, stands for the key parameter in the volume-penalization approach. For vanishing η , the solution \tilde{u}_i of the penalized equations (2.4) and (2.5) converges to the solution u_i of the original equations (2.1) and (2.2) with the global penalty error scaling as $\eta^{1/2}$ in Ω_f (Carbou & Fabrie 2003). Thus, the no-slip boundary condition (2.3) can be enforced to any high accuracy by appropriately reducing η , but at the cost of increasing the stiffness of the penalized momentum equation (2.5). However, due to its diagonal nature, the penalty term can be easily solved implicitly, while explicit treatment of the penalization term would require an integration time step of order η .

When dealing with incompressible flow past obstacles, the evaluation of the aerodynamic force is the most important issue. To this end, the Brinkman volume penalization shows a fundamental advantage with respect to other methods of solution. Specifically, the force acting on the obstacle can be simply evaluated as

$$F_i(t) = \frac{\rho}{\eta} \int_{\Omega_s} (\tilde{u}_i + U_i) \, d\mathbf{x}, \quad (2.7)$$

i.e. by integrating the total velocity field over the volume occupied by the obstacle (Angot *et al.* 1999).

Generally, the continuity (2.4) and penalized momentum (2.5) equations could be solved with any numerical technique. In this work, the efficient combination of the volume-penalization approach with the AWC solver is exploited (Kevlahan & Vasilyev 2005).

2.2. The adaptive wavelet collocation method

In the context of AWC methodology (Vasilyev & Bowman 2000), the governing equations (2.4) and (2.5) are evaluated at collocation points, which leads to a set of nonlinear ordinary differential equations for the collocated unknowns. The method allows the numerical grid not to be fixed once for all, but dynamically adapted in time, following the evolution of the flow structures, in both location and scale. That is, the mesh adaptation is obtained through the use of nested wavelet grids, due to the one-to-one correspondence between wavelets and grid points. Higher-resolution computations are in fact conducted where and only where sharper gradients occur in the flow field.

The separation between resolved flow structures and unresolved residual flow is obtained through nonlinear multiresolution wavelet threshold filtering (WTF). The filtering operation is defined by applying the wavelet transform to the unfiltered field, zeroing the wavelet coefficients below a given threshold, say ϵ , and transforming back

to the physical space (e.g. Farge, Schneider & Kevlahan 1999). The procedure results in the decomposition of the velocity field into two different parts: a coherent more energetic field and a residual less energetic coherent/incoherent one, i.e. $\tilde{u}_i = \tilde{u}_i^{>\epsilon} + \tilde{u}'_i$, where $\tilde{u}_i^{>\epsilon}$ stands for the wavelet-filtered perturbation velocity, which is formally represented by

$$\tilde{u}_i^{>\epsilon}(\mathbf{x}) = \sum_{l \in \mathcal{L}^1} c_l^1 \phi_l^1(\mathbf{x}) + \sum_{j=1}^{+\infty} \sum_{\mu=1}^{2^3-1} \sum_{\substack{\mathbf{k} \in \mathcal{K}^{\mu,j} \\ |d_k^{\mu,j}| > \epsilon \|\tilde{u}_i\|}} d_k^{\mu,j} \psi_k^{\mu,j}(\mathbf{x}). \quad (2.8)$$

In the above expression, bold subscripts denote three-dimensional indices, while \mathcal{L}^1 and $\mathcal{K}^{\mu,j}$ are three-dimensional index sets associated with scaling functions ϕ_l^1 and wavelets $\psi_k^{\mu,j}$ respectively. Each level of resolution j consists of wavelets belonging to the same family μ , having the same scale but located at different grid positions. Collocation points are in fact omitted from the computational grid if the associated wavelets are omitted from the representation (2.8), which occurs when the corresponding coefficients are below the given thresholding level. In a practical calculation, the choice of the maximum resolution, which corresponds to the finest allowable wavelet grid, is dictated by the physically required spatial resolution as well as the acceptable computational cost.

Depending on the choice of the parameter ϵ , only a small fraction of the available wavelets are used in representing the velocity field \tilde{u}_i , which results in the characteristic compression property of wavelet-based methods, e.g. Schneider & Vasilyev (2010). It should be mentioned that the adaptive grid also contains points corresponding to wavelets that are not significant but could become significant during a single step of the time integration. The necessary use of adjacent wavelets causes a partial detriment to the grid compression, which, however, remains very high. It should be noted that despite the three to five times increase in per-point computational cost, the AWC method is still more efficient than the corresponding non-adaptive approach, mainly due to high grid compression. In fact, even with the inclusion of adjacent wavelets, the fraction of wavelet collocation points that are needed to satisfactorily represent the solution always remains significantly lower than 20%. The latter represents the percentage of active wavelets for which the computational costs of adaptive and non-adaptive methods would be comparable. Usually, the percentage is well under this limit, as occurs for the numerical experiments presented in this work.

When the AWC method is combined with the volume-penalization technique discussed in the previous section, the presence of solid obstacles is automatically taken into account by the adaptive computational mesh. In this case, in addition to adapting on the penalized velocity field one may also adapt on the discontinuous mask function χ_s .

The AWC method has the ability to unambiguously identify and isolate localized dynamically dominant flow structures and to track them on adaptive computational meshes (Schneider & Vasilyev 2010). Indeed, the AWC method is particularly effective in the simulation of shedding flow past bluff bodies. Differently from the classical zonal mesh approach, where the numerical grid is *a priori* designed to resolve the main flow structures in the wake region, regardless of the instantaneous vorticity distribution, the wavelet-based adaptation allows the grid to be continuously modified in time in order to follow the evolution of the wake.

One of the main strengths of the present hybrid method lies in the direct control of the solution errors. On the one hand, the penalization error is regulated by the parameter η , while on the other hand the numerical accuracy is controlled through the thresholding level ϵ in wavelet decomposition (2.8). Therefore, the desired level of approximation can be achieved by appropriately prescribing these two parameters. It is worth stressing that, due to the existence of a thin boundary layer inside the obstacle domain Ω_s , the thickness of which is proportional to $(\eta\nu)^{1/2}$, e.g. Keetels *et al.* (2007), the necessary numerical resolution increases with the fictitious solidness of the obstacle. Hence, given the fluid viscosity, the thresholding level ϵ cannot be chosen independently from the penalty constant η , but should decrease with it.

The choice of the threshold ϵ determines the relative energy level of the eddies that are resolved and, consequently, controls the importance of the residual field associated with the discarded wavelets. In principle, a very low but non-zero value for this parameter can be prescribed so that the effect of unresolved motions can be completely ignored and the wavelet-based direct numerical solution of the penalized equation (2.5) is carried out, where $\tilde{u}_i \cong \tilde{u}_i^{>\epsilon}$. Even though the number of degrees-of-freedom of the WDNS is strongly reduced compared to non-adaptive DNS and the Reynolds number scaling is improved compared with conventional estimates (Kevlahan, Alam & Vasilyev 2007; Nejadmalayeri, Vezolainen & Vasilyev 2013), the computational cost still remains very high even at moderately large Reynolds number, thus, necessitating the use of turbulence modelling approaches.

2.3. The penalized adaptive LES approach

The computational cost of WDNS can be substantially reduced if higher thresholding levels are adopted. In this case the wavelet decomposition (2.8) must be interpreted as the definition of the wavelet-filtered velocity field, $\tilde{u}_i^{>\epsilon}$, which is actually solved for, while the influence of the residual velocity field on the dynamics of the resolved eddies cannot be neglected and must be modelled, resulting in the wavelet-based adaptive LES approach.

The governing equations for adaptive LES are formally obtained by applying the WTF operator to the incompressible Navier–Stokes equations, followed by the divergence-free projection, which leads to the following continuity and momentum equations:

$$\frac{\partial \tilde{u}_i^{>\epsilon}}{\partial x_i} = 0, \quad (2.9)$$

$$\frac{\partial \tilde{u}_i^{>\epsilon}}{\partial t} + \left(\tilde{u}_j^{>\epsilon} + U_j \right) \frac{\partial \tilde{u}_i^{>\epsilon}}{\partial x_j} = - \frac{\partial \tilde{P}^{>\epsilon}}{\partial x_i} + \nu \frac{\partial^2 \tilde{u}_i^{>\epsilon}}{\partial x_j \partial x_j} - \frac{\chi_s}{\eta} \left(\tilde{u}_i^{>\epsilon} + U_i \right) - \frac{\partial \tau_{ij}}{\partial x_j}, \quad (2.10)$$

where $\tau_{ij} = \overline{\tilde{u}_i \tilde{u}_j^{>\epsilon}} - \tilde{u}_i^{>\epsilon} \tilde{u}_j^{>\epsilon}$ stands for the unknown residual stresses to be modelled. It is worth noting that the bar used in the notation of the kinematic pressure variable $\tilde{P}^{>\epsilon}$ does not imply the application of the WTF operator, but is used for consistency with the other terms. Instead, the pressure term on the right-hand side of (2.10) must be viewed as a Lagrange multiplier enforcing the incompressibility constraint (2.9). Moreover, it should be mentioned that, as occurs for LES with non-uniform filter width (Vasilyev, Lund & Moin 1998), there is a commutation error between WTF and derivative operators, the effect of which is not considered here.

However, the commutation error is significantly reduced by using the adjacent zone (Schneider & Vasilyev 2010).

Different modelling procedures that have been developed for wavelet-based LES can be used for bluff body flows, e.g. Vasilyev *et al.* (2008). In this study, the filtered momentum equations are closed by means of the localized dynamic kinetic-energy-based model (LDKM) proposed in De Stefano, Vasilyev & Goldstein (2008). Specifically, the deviatoric part of the residual stress tensor is approximated according to the eddy-viscosity assumption, i.e.

$$\tau_{ij}^* \cong -2\nu_t \overline{\overline{S_{ij}^{>\epsilon}}} \quad (2.11)$$

where

$$\overline{\overline{S_{ij}^{>\epsilon}}} = \frac{1}{2} \left(\frac{\partial \overline{\overline{u_i^{>\epsilon}}}}{\partial x_j} + \frac{\partial \overline{\overline{u_j^{>\epsilon}}}}{\partial x_i} \right)$$

is the resolved rate-of-strain tensor. The turbulent eddy viscosity $\nu_t = C_\nu \Delta k_{sgs}^{1/2}$ depends on the subgrid-scale kinetic energy, $k_{sgs} = (1/2)\tau_{ii}$, and the known local wavelet filter width, Δ , while C_ν stands for a dimensionless model parameter.

The model transport equation for the SGS kinetic energy field is derived from the momentum equations (2.5) and (2.10) and can be written as

$$\frac{\partial k_{sgs}}{\partial t} + (\overline{\overline{u_j^{>\epsilon}}} + U_j) \frac{\partial k_{sgs}}{\partial x_j} = \nu \frac{\partial^2 k_{sgs}}{\partial x_j \partial x_j} + \frac{\partial}{\partial x_j} \left(\nu_t \frac{\partial k_{sgs}}{\partial x_j} \right) + \Pi - \epsilon_{sgs} - \frac{\chi_s}{\eta} (2k_{sgs}), \quad (2.12)$$

where $\Pi = -\tau_{ij}^* \overline{\overline{S_{ij}^{>\epsilon}}} \cong 2\nu_t \overline{\overline{S_{ij}^{>\epsilon}}} \overline{\overline{S_{ij}^{>\epsilon}}}$ represents the dissipation of resolved energy, which is the rate at which energy is transferred from resolved motions to unresolved ones. It is important to note that the fraction of unresolved turbulent eddies and, thus, the amount of SGS dissipation increases with the thresholding level (Goldstein & Vasilyev 2004).

The dissipation rate of the SGS kinetic energy, which is defined as

$$\epsilon_{sgs} = \nu \left(\frac{\partial \overline{\overline{u_i^{>\epsilon}}}}{\partial x_j} \frac{\partial \overline{\overline{u_i^{>\epsilon}}}}{\partial x_j} - \frac{\partial \overline{\overline{u_i^{>\epsilon}}}}{\partial x_j} \frac{\partial \overline{\overline{u_j^{>\epsilon}}}}{\partial x_j} \right), \quad (2.13)$$

is approximated using simple scaling arguments as $\epsilon_{sgs} \cong C_\epsilon k_{sgs}^{3/2} / \Delta$, where C_ϵ stands for the second dimensionless model parameter. Both the coefficients C_ν and C_ϵ are determined as space–time functions following either a Germano-like or a Bardina-like dynamic approach (De Stefano *et al.* 2008). It is worth stressing that the parameter C_ν can take negative values, thus, accounting for local backscatter that represents a transfer of energy from SGS to resolved motions.

The evolution equation (2.12) is solved together with the filtered momentum equation (2.10) and the associated incompressibility constraint (2.9) using the AWC numerical method. It is worth noting that the variable k_{sgs} is penalized in such a way that it vanishes inside the volume occupied by the solid obstacle. This fact leads to the introduction of the additional penalization term in (2.12) with respect to the original LDKM formulation proposed in De Stefano *et al.* (2008) and De Stefano & Vasilyev (2010) for freely decaying and forced homogeneous turbulence. The coefficient 2 in the last term of the penalized k_{sgs} equation is used for consistency with the momentum equations (2.5) and (2.10).

3. Square cylinder flow

The combined method presented in the previous section is applied to the simulation of vortex shedding flow behind a stationary right prism with square cross-section, immersed in a uniform fluid stream. Naturally, the constant free stream speed U and the side length of the square section L are used as the reference velocity and reference length, respectively. By prescribing a unitary value for both these quantities, the following non-dimensional filtered momentum equations are solved in practice:

$$\frac{\partial \bar{u}_i^{>\epsilon}}{\partial t} + \left(\bar{u}_j^{>\epsilon} + U_j \right) \frac{\partial \bar{u}_i^{>\epsilon}}{\partial x_j} = - \frac{\partial \bar{P}^{>\epsilon}}{\partial x_i} + \frac{1}{Re} \frac{\partial^2 \bar{u}_i^{>\epsilon}}{\partial x_j \partial x_j} - \frac{\chi_s}{\bar{\eta}} \left(\bar{u}_i^{>\epsilon} + U_i \right) - \frac{\partial \tau_{ij}}{\partial x_j}, \quad (3.1)$$

where $Re = UL/\nu$ is the mean flow Reynolds number and $\bar{\eta} = \eta U/L$ represents the non-dimensional penalization coefficient. It should be noted that, for the sake of simplicity, non-dimensional variables in (3.1) are denoted by the same symbols as those used for the corresponding dimensional quantities in (2.10). Inside the obstacle domain, where $\chi_s = 1$, the penalization term has the same importance as the viscous term in a thin boundary layer with non-dimensional thickness of order $(\bar{\eta}/Re)^{1/2}$.

The flow around the two-dimensional obstacle is described in a Cartesian coordinate system (x, y, z) , where the first axis corresponds to the inlet flow direction and the third one coincides with the cylinder spanwise direction. The square cross-section is aligned with the first two axes. The computational domain is chosen to be $\Omega = [-x_{in}, x_{out}] \times [-h/2, h/2] \times [-b/2, b/2]$, where h and b represent the lateral and spanwise non-dimensional extents, respectively, while the domain occupied by the cylinder is $\Omega_s = [-1/2, 1/2] \times [-1/2, 1/2] \times [-b/2, b/2]$. The lateral dimension of the domain defines the solid blockage parameter, that is $\beta = 1/h$. The spatial discretization is performed by using a given number J of nested wavelet collocation grids, with $\Delta x = \Delta y = \delta$ and $\Delta z = 2\delta$, where the mesh spacing varies according to $\delta = 2^{-j+1}$, with $1 \leq j \leq J$.

The penalized momentum equations (3.1) are solved in Ω , supplied with the following boundary conditions for the unknown perturbation velocity field $\bar{u}_i^{>\epsilon}$ on $\partial\Omega$. Zero-velocity conditions are imposed at the inflow boundary ($x = -x_{in}$), while convective conditions are prescribed at the outflow boundary ($x = x_{out}$), namely,

$$\frac{\partial \bar{u}_i^{>\epsilon}}{\partial t} + \left(\bar{u}_1^{>\epsilon} + 1 \right) \frac{\partial \bar{u}_i^{>\epsilon}}{\partial x} = 0. \quad (3.2)$$

Moreover, free-slip conditions are imposed at the lateral boundaries ($y = \pm h/2$), i.e. $\partial \bar{u}_1^{>\epsilon} / \partial y = \bar{u}_2^{>\epsilon} = \partial \bar{u}_3^{>\epsilon} / \partial y = 0$, and periodicity is assumed in the homogeneous spanwise direction ($z = \pm b/2$). According to (2.7), the time-dependent spanwise-averaged drag and lift coefficients are given by

$$C_D(t) = \frac{2}{\bar{\eta}b} \int_{\Omega_s} \left(\bar{u}_1^{>\epsilon} + 1 \right) dx, \quad (3.3)$$

and

$$C_L(t) = \frac{2}{\bar{\eta}b} \int_{\Omega_s} \bar{u}_2^{>\epsilon} dx, \quad (3.4)$$

respectively.

In the adaptive LES approach, the SGS kinetic energy equation (2.12) is solved starting from a uniform very low but non-zero value k_0 , which is also used as the inflow condition. For the k_{sgs} variable, homogeneous Neumann conditions are enforced at the lateral boundaries, periodicity is assumed in the spanwise direction and convective outflow boundary conditions are used, analogously to (3.2).

4. Numerical experiments

In order to test the proposed simulation methodology for square cylinder flow, some numerical experiments are carried out for two different flow configurations. Wavelet-based direct numerical simulation solutions are obtained at low supercritical Reynolds number, i.e. $Re = 200$, by fully resolving the three-dimensional structure of the cylinder wake, while adaptive LES solutions are provided at higher Reynolds number, i.e. $Re = 2000$, by supplying the simulation with the LDKM model briefly reviewed in § 2.3. In both cases, the non-dimensional extent of the computational domain in the streamwise direction is assumed with $x_{in} = 6$ and $x_{out} = 18$. It is worth noting that all the numerical solutions have been obtained by employing a fourth-order spatial discretization, the linearized Crank–Nicolson split-step time integration method with adaptive time stepping (Kevlahan & Vasilyev 2005) and the parallel version of the AWC solver, which has been recently developed (Nejadmalayeri 2012).

4.1. The WDNS solution

The computational domain for the WDNS experiments is chosen to have spanwise and lateral non-dimensional extents that are $b = 6$ and $h = 18$, respectively. The present length-to-width ratio of the cylinder represents a good compromise between the requirement to accommodate a meaningful number of secondary vortices in the spanwise direction and the need to save computational resources. However, as demonstrated by Sohankar *et al.* (1999), at moderate Reynolds numbers, the use of higher spanwise extensions has small effects on the global results. The AWC solver is used with a thresholding level $\epsilon = 5 \times 10^{-3}$, while no modelling procedure is employed for the residual stresses. Practically, the non-dimensional equations corresponding to the unfiltered penalized momentum equation (2.5) are solved, where the penalization coefficient is prescribed as $\bar{\eta} = 10^{-3}$. The numerical solution is obtained starting from zero perturbation velocity as the initial condition and conducting the computation until the wake is fully developed and periodical vortex shedding occurs. The incoming flow is undisturbed and the wake transitional process is naturally promoted by the numerical truncation errors.

Seven levels of resolution are employed for the WDNS solution. The range of effective mesh sizes is similar to that used in analogous studies at comparable Reynolds numbers, e.g. Sohankar *et al.* (1999), the highest level of resolution corresponding to $\delta_{min} = 1/64$. Differently from similar studies, however, the non-uniform mesh spacing is not prescribed *a priori*, but dynamically determined according to the flow evolution. In particular, close to the body surface, the local resolution is dictated by the high gradients of the mask function χ_s and, thus, the finest wavelet collocation grid is used. Due to the moderately low Reynolds number, the prescribed maximum resolution is adequate to resolve the kinematic boundary layer inside the fluid region. Theoretically, the same resolution does not suffice for the description of the boundary layer that exists inside the obstacle. However, in practice, as occurred in similar studies, e.g. Keetels *et al.* (2007), the present

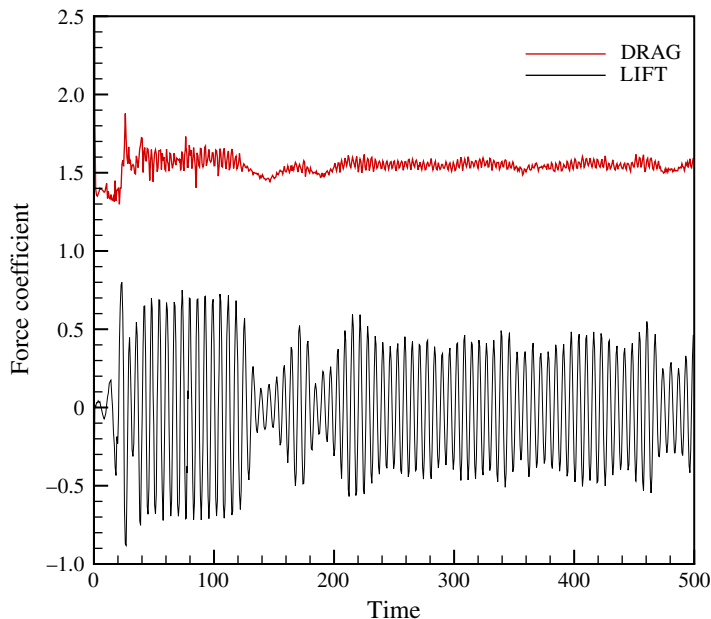


FIGURE 1. (Colour online) The WDNS solution at $Re = 200$: time history of the spanwise-averaged force coefficients.

numerical experiments provide completely acceptable results, without resorting to the use of extremely refined grids that fully resolve the inner boundary layer.

After a transient period, during which the wake develops from initial free-stream conditions, the aerodynamic forces exhibit the classical oscillatory behaviour of bluff body flows, as illustrated in figure 1, where the time histories of the spanwise-averaged drag (3.3) and lift (3.4) coefficient are reported. The time statistics, which are accumulated for fully developed vortex shedding flow, are as follows. The time-averaged drag coefficient is $\bar{C}_D = 1.57$ and the associated root-mean-square is $C'_D = 0.034$ while, for the lift coefficient, it holds that $|\bar{C}_L| = 0.007$ and $C'_L = 0.366$. The power spectra of both the force coefficients are depicted in figure 2. By looking at the spectrum for the lift coefficient, it is apparent that the fundamental frequency f_0 of vortex shedding corresponds to the Strouhal number $St = f_0 L/U = 0.158$. On the other hand, the spectrum for the drag coefficient, which clearly shows a peak at zero frequency, demonstrates that the drag force fluctuates at twice the shedding frequency, $2f_0$, as well as at $4f_0$. The characteristic intermittent low-frequency modulation, which is apparent in both the drag and the lift plots, relates to the process of vortex dislocation that appears randomly in space and time. During the period of a dislocation the drag coefficient, as well as the modulus of the lift coefficient, markedly decreases (Williamson 1996).

The present results are in good agreement with experimental findings (Luo *et al.* 2003) as well as with data from reference non-adaptive numerical simulations (Robichaux *et al.* 1999; Saha, Biswas & Muralidhar 2003), as demonstrated in table 1. The accordance with reference data can even be improved by increasing the numerical accuracy, as demonstrated in the following. The discrepancy with results presented in Sohankar *et al.* (1999) can be attributed to the second-order accuracy

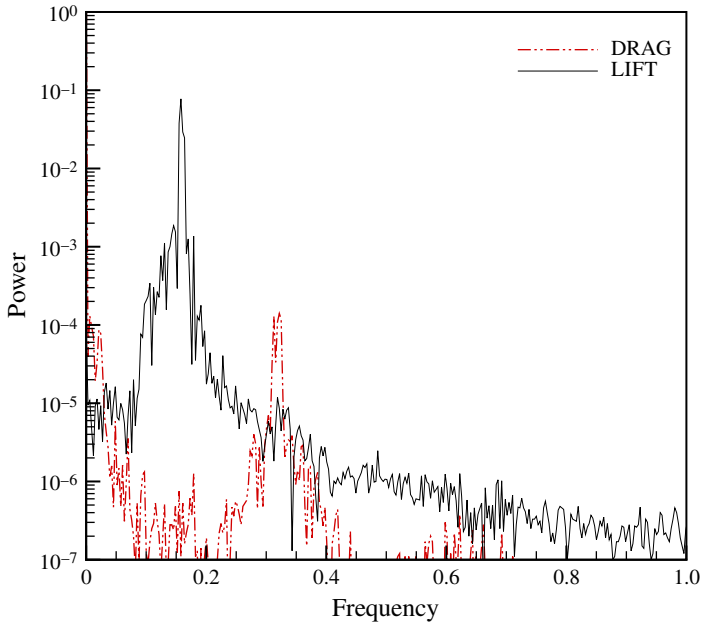


FIGURE 2. (Colour online) The WDNS solution at $Re = 200$: power spectrum of the spanwise-averaged force coefficients.

Case	\bar{C}_D	C'_D	C'_L	St
Present study	1.57	0.034	0.366	0.158
Robichaux <i>et al.</i> (1999)	1.64	—	—	0.157
Saha <i>et al.</i> (2003)	1.67	0.026	0.305	0.163
Sohankar <i>et al.</i> (1999)	1.39	0.032	0.210	0.157
Luo <i>et al.</i> (2003)	—	—	—	0.159

TABLE 1. The WDNS solution at $Re = 200$: validation of the present integral results against computational data from reference non-adaptive numerical simulations and experimental results.

and low spanwise resolution of the finite volume method used in that work, given the same blockage ratio, that is $\beta = 1/18$.

The complex flow scenario existing at the present transitional Reynolds number is illustrated by examining the vorticity field at two different time instants, which correspond to periods of low and high aerodynamic force. The contour maps of the spanwise vorticity component in three different planes ($z = -2.8, 0$ and 2.8) are depicted in figure 3(a,c) for the range $-2 < \omega_z < 2$. Furthermore, the contours of the transverse vorticity component in the planes $y = -1, 0$ and 1 are reported in figure 4 for the range $-0.5 < \omega_y < 0.5$, while the streamwise vorticity field in the planes $x = 2.5, 5.5, 8.5$ and 11.5 is illustrated in figure 5 for the range $-0.5 < \omega_x < 0.5$. It is worth noting, in particular, the sign periodicity existing in both the streamwise and the spanwise direction. The present figures are in accordance with results from different numerical solutions like those by Sohankar *et al.* (1999) and Saha *et al.* (2003),

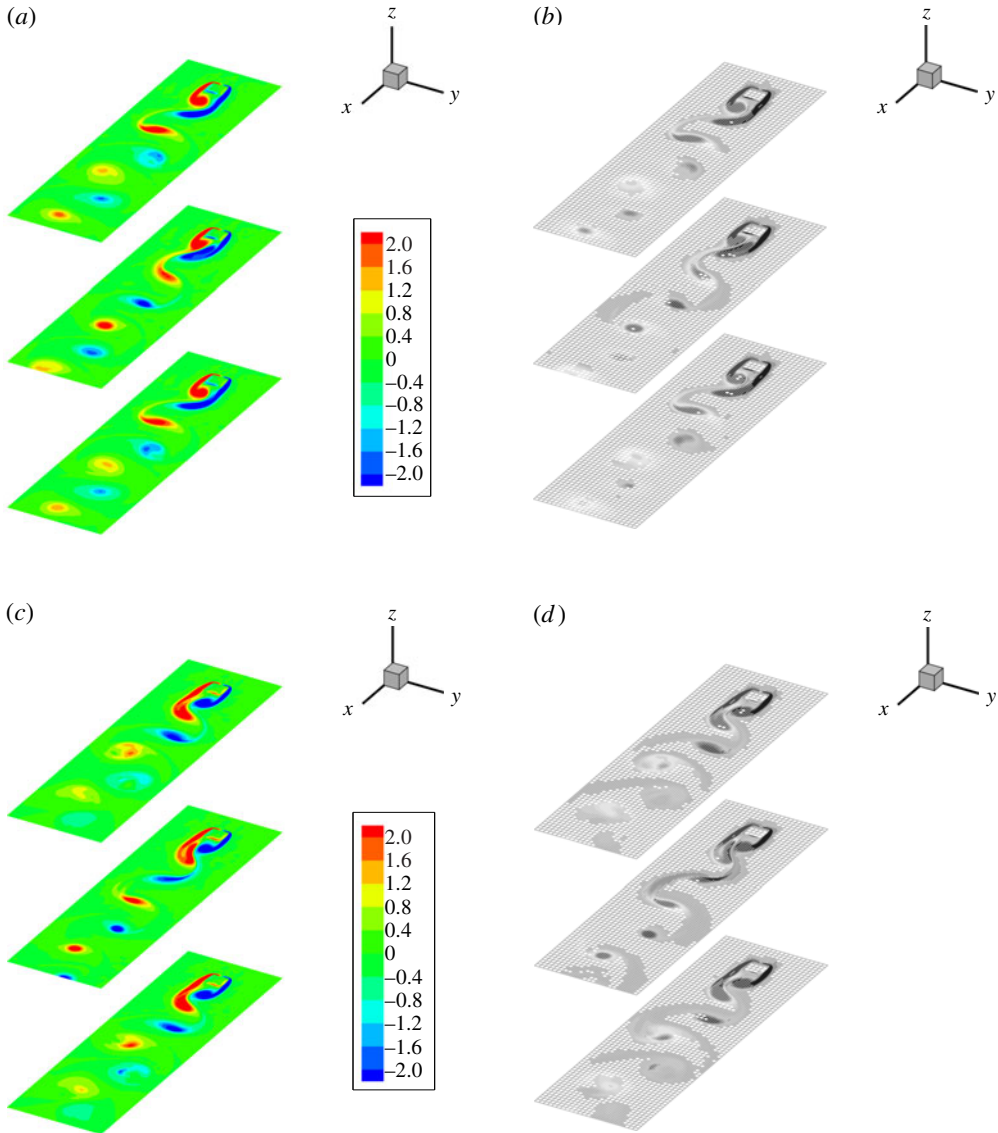


FIGURE 3. The WDNS solution at $Re = 200$: spanwise vorticity contours ($-2 < \omega_z < 2$) (a,c) and computational mesh (b,d) in the planes $z = -2.8, 0$ and 2.8 , at two different time instants corresponding to phases of high (a,b) and low (c,d) force. Close-up view in the domain $-2 < x < 17$, $-3 < y < 3$.

among others. In panels (b) and (d) of the above figures, the corresponding slices of the adaptive computational mesh are reported at the same time instants, demonstrating how the AWC method is able to closely follow the space–time evolution of the wake.

Furthermore, in order to present a clear three-dimensional view of the cylinder wake, the main vortical structures can be identified according to the Q -criterion (Hunt, Wray & Moin 1988), which exploits the second invariant of the velocity gradient tensor, $Q \equiv 1/2(\Omega_{ij}\Omega_{ij} - S_{ij}S_{ij})$, where Ω_{ij} and S_{ij} stand for the rate-of-rotation and

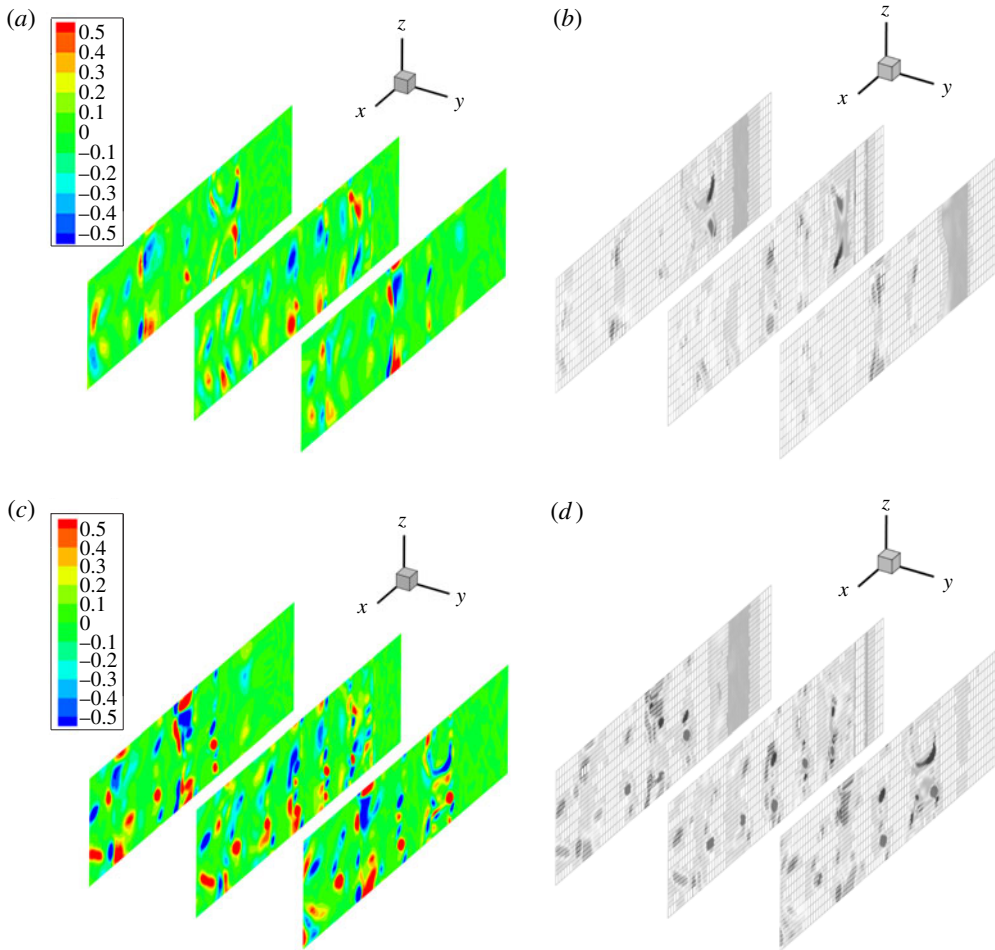


FIGURE 4. The WDNS solution at $Re = 200$: transverse vorticity contours ($-0.5 < \omega_y < 0.5$) (*a,c*) and computational mesh (*b,d*) in the planes $y = -1, 0$ and 1 , at two different time instants corresponding to phases of high (*a,b*) and low (*c,d*) force. Close-up view in the domain $-2 < x < 17$, $-3 < z < 3$.

rate-of-strain tensors, respectively. The method, which simply defines a vortex as a connected region where $Q > 0$, is particularly suitable for the examination of separated flows, e.g. De Stefano, Denaro & Riccardi (1998) and Dubief & Delcayre (2000). The evolution of the square cylinder wake is illustrated in figure 6, by reporting four different images at four different time instants equally spaced over a shedding period. In panels (*a,c,e,g*), the isosurfaces of $Q = 0.1$ and 0.3 are drawn, where the translucency of the isosurfaces corresponding to the lower value of Q allows the vortex cores to be clearly visualized. In panels (*b,d,f,h*) of the same figure, the scatter plots of the collocation points associated with the retained wavelets, corresponding the same time instants, are depicted. Since all the wavelets belonging to the coarser levels of resolution with $1 \leq j \leq 3$ are actually kept throughout the computational domain, for the sake of

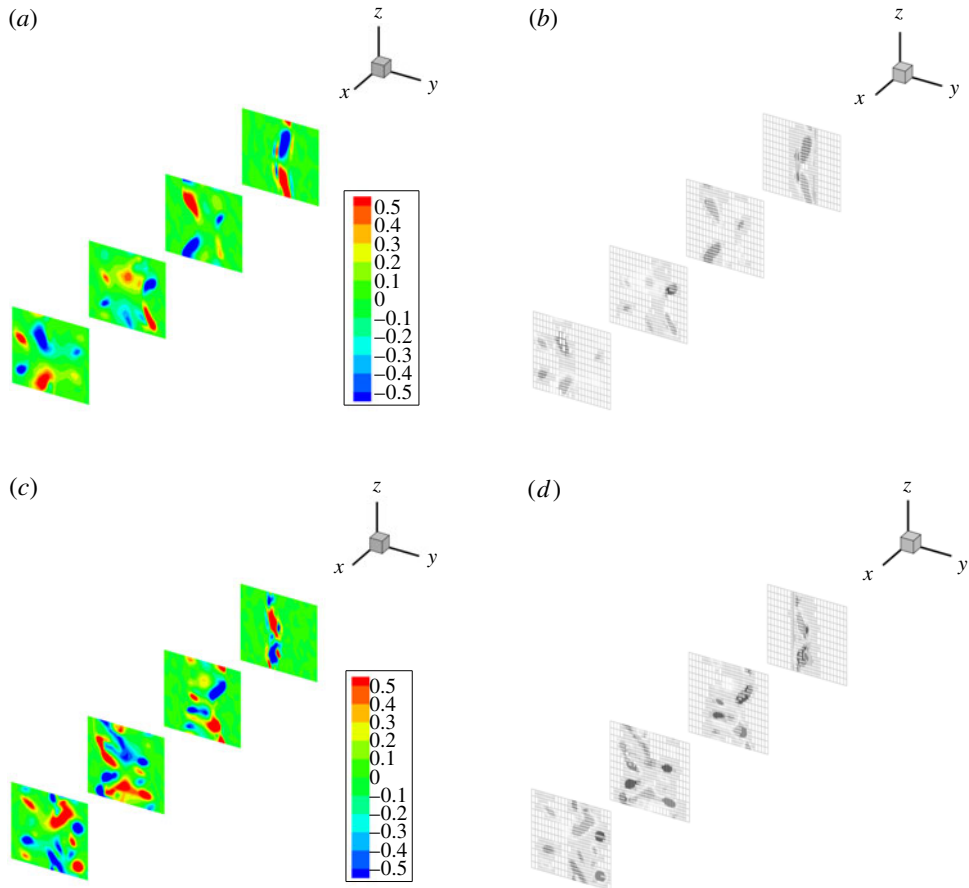


FIGURE 5. The WDNS solution at $Re = 200$: streamwise vorticity contours ($-0.5 < \omega_x < 0.5$) (a,b) and computational mesh (b,d) in the planes $x = 2.5, 5.5, 8.5$ and 11.5 , at two different time instants corresponding to phases of high (a,b) and low (c,d) force. Close-up view in the domain $-3 < y < 3$, $-3 < z < 3$.

clarity the scatter plot, which is coloured by the variable grid level, is reported only for $4 \leq j \leq 7$.

By inspection of these figures, it is apparent that the flow dynamics is governed by the vortical structures that are shed from the cylinder and are convected downstream, while secondary vortices are generated in the near wake. During a high-force phase, the wake is characterized by the presence of large spanwise vortices. Eventually, these structures are destroyed and, during a low-force phase, the wake shows a complex three-dimensional shape due to symmetric two-sided dislocation. It is evident that the spatial distribution of active wavelet collocation points closely resembles that of the main vortical structures.

In fact, the number and the spatial distribution of the retained wavelet collocation points follow the evolution of the shedding flow. During a period of high force, the rather simple wake can be simulated by using a relatively low number of wavelets. In contrast, during a period of low force, which corresponds to a very complex shape of the wake, many more grid points are included in the computation as the wavelet

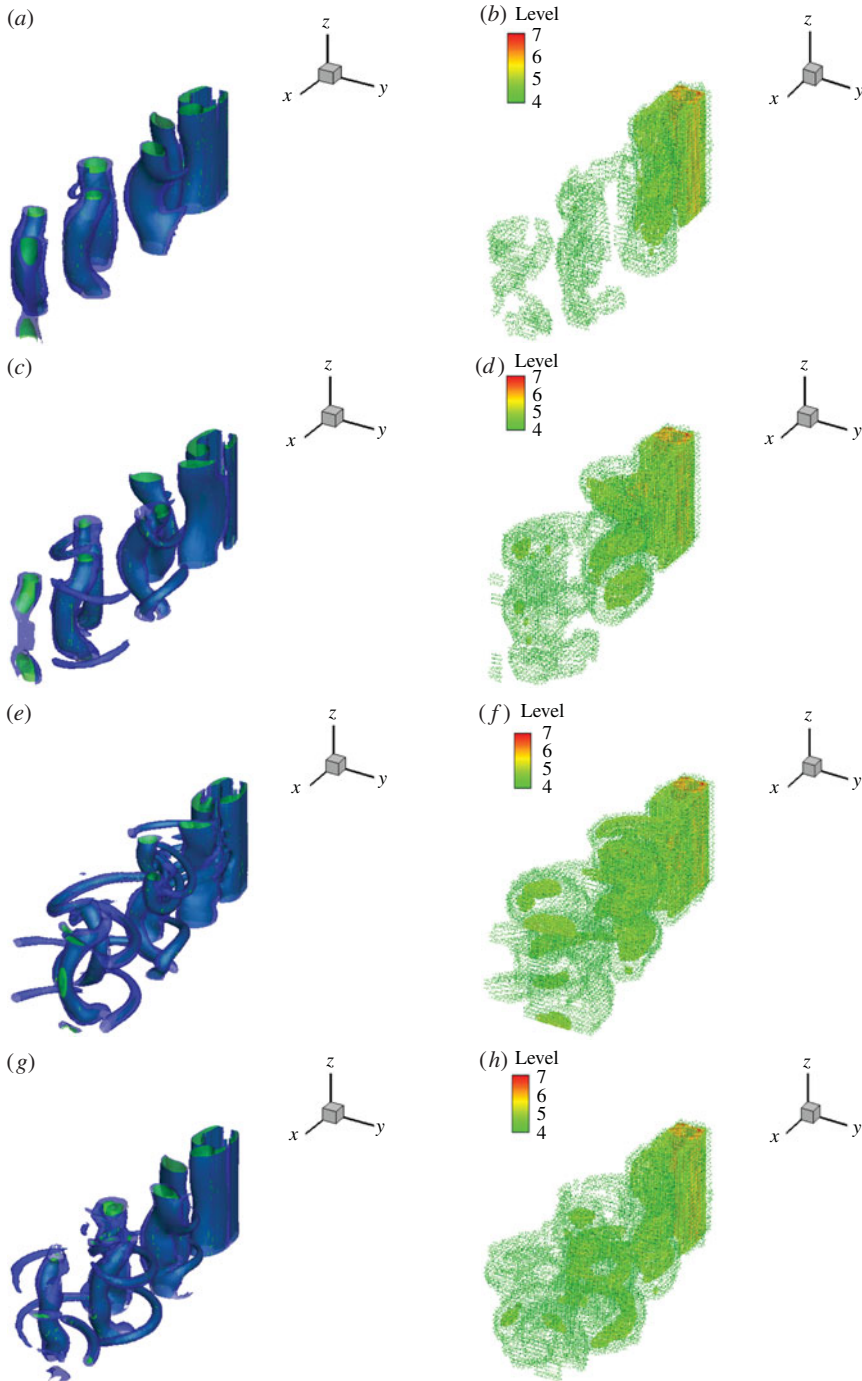


FIGURE 6. The WDNS solution at $Re = 200$: main vortical structures identified by the isosurfaces of $Q = 0.1$ (blue) and 0.3 (green), (a,c,e,g) and scatter plot of the wavelet collocation points at higher levels of resolution ($4 \leq j \leq 7$), (b,d,f,h) at four different time instants equally spaced over a shedding period. Close-up view in the domain $-2 < x < 17$, $-3 < y < 3$, $-3 < z < 3$.

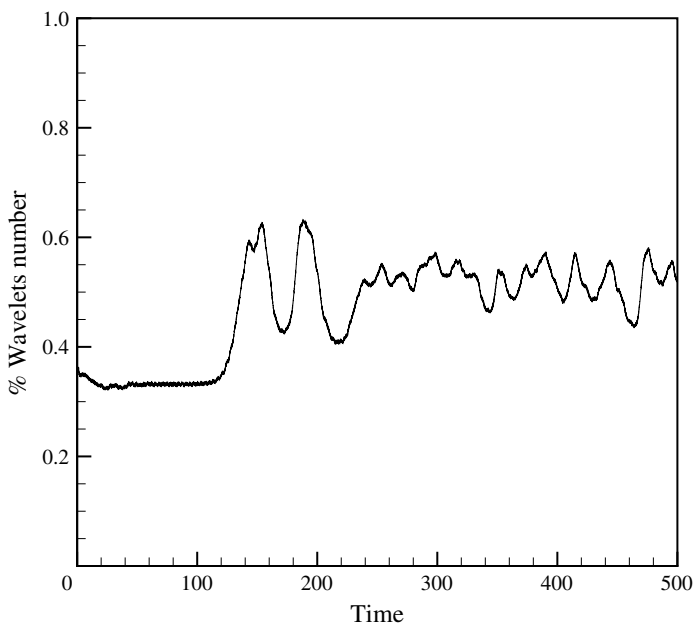


FIGURE 7. The WDNS solution at $Re = 200$: time history of the percentage of active wavelets.

collocation grid is automatically refined where smaller vortical structures are created. The time history of the percentage of active wavelets, including those belonging to the adjacent zone, is shown in figure 7. After the initial transient period, the number of retained wavelets reflects the oscillations of the wake-induced forces and, due to the high compression property of the AWC method, a very low fraction (less than 0.7%) of the total number of available wavelets on the finest grid is actually involved in the calculation.

In order to illustrate the convergence properties of the proposed WDNS method, some additional experiments are performed by varying the wavelet thresholding level ϵ and the number of levels of resolution J of the wavelet collocation grids (or, equivalently, the minimum available mesh spacing δ_{min}) that is used. These calculations are carried out starting from the velocity field provided by the WDNS solution discussed above, with $\epsilon = 5 \times 10^{-3}$ and $J = 7$ (case I), at a given time instant corresponding to developed flow conditions. To evaluate the new time statistics, the numerical data are accumulated for a period corresponding to five shedding cycles. By inspection of table 2, where the global results of the different simulations are summarized, the aerodynamic force quantities can be seen to converge towards limiting values with increasing numerical accuracy, by decreasing either the wavelet threshold (case II) or the mesh spacing (case III). In particular, the drag coefficient appears to be slightly underestimated and, to achieve effective grid independence, the numerical resolution should be further increased.

As the choice of the penalization coefficient has a significant influence on the solution, the effect of selecting a different value for this parameter is also investigated by conducting two extra computations with $\bar{\eta} = 5 \times 10^{-4}$ (cases IV and V). It turns out that, for a prescribed numerical resolution (fixed ϵ and J), the grid compression

Case	ϵ	δ_{min}	$\bar{\eta}$	\bar{C}_D	C'_D	$ \bar{C}_L $	C'_L	St
I	5×10^{-3}	2^{-6}	1×10^{-3}	1.57	0.034	0.007	0.366	0.158
II	1×10^{-3}	2^{-6}	1×10^{-3}	1.60	0.030	0.040	0.368	0.159
III	5×10^{-3}	2^{-7}	1×10^{-3}	1.61	0.033	0.017	0.364	0.159
IV	5×10^{-3}	2^{-6}	5×10^{-4}	1.52	0.064	0.003	0.361	0.158
V	1×10^{-3}	2^{-6}	5×10^{-4}	1.56	0.034	0.028	0.368	0.159

TABLE 2. The WDNS solution at $Re = 200$: summary of the integral results for different values of the wavelet threshold ϵ , the minimum mesh spacing δ_{min} and the penalization parameter $\bar{\eta}$.

is practically unaffected by changing this parameter. This is not surprising however, because the finest wavelet grid is involved in the neighbourhood of the fictitious fluid–body interface. Theoretically, the penalty error decreases with the penalization parameter and the accuracy of the solution should improve for lower $\bar{\eta}$. In practice, due to the existence of a boundary layer inside the porous region, the thickness of which scales with $\bar{\eta}^{1/2}$, the wavelet thresholding level must decrease with the penalization coefficient, in order to maintain the desired numerical accuracy. When this is not the case, the quality of the solution deteriorates, as occurs for case IV, where the drag coefficient, for instance, appears to be strongly underestimated.

Finally, the vortex shedding frequency, represented by the Strouhal number, is practically the same for all the simulations that are conducted.

4.2. The adaptive LES solution

The adaptive LES solution of square cylinder flow at $Re = 2000$ is obtained by solving the filtered governing equation (3.1), supplied with the LDKM model. Given the increased Reynolds number, eight levels of resolution are used, so that the minimum mesh size corresponds to $\delta_{min} = 1/128$, while the penalization coefficient is prescribed as $\bar{\eta} = 5 \times 10^{-4}$. The computational domain for the LES experiment is prescribed to have spanwise and lateral non-dimensional extents of $b = 4$ and $h = 16$, respectively. The instantaneous velocity field corresponding to the no-model solution at $Re = 200$ is taken as the initial condition, and the modelled computation is conducted until the vortex shedding flow reaches new fully developed conditions.

The non-dimensional SGS energy equation is solved by choosing $k_0 = 10^{-8}$ for the associated initial and boundary conditions. Two different experiments are carried out, where the model coefficients are determined by means of either the Germano-like (LDKM-G) or the Bardina-like (LDKM-B) dynamic procedure.

In the framework of the present wavelet-based LES approach, the threshold ϵ in decomposition (2.8) stands for the user-defined key parameter that reflects the desired level of turbulence resolution, by determining the relative importance of resolved and modelled turbulent eddies. In a practical calculation, this parameter can be chosen by referring to previous studies at comparable Reynolds numbers. In this work, an LES solution is obtained, for instance, by fixing $\epsilon = 0.15$ as the wavelet filtering threshold. It is worth noting that the grid compression remains very high, however, being higher than in the previous WDNS case. The actual turbulence resolution that can be measured by the percentage of modelled SGS dissipation to the total dissipation (modelled SGS plus resolved viscous dissipation) is about 11% in the

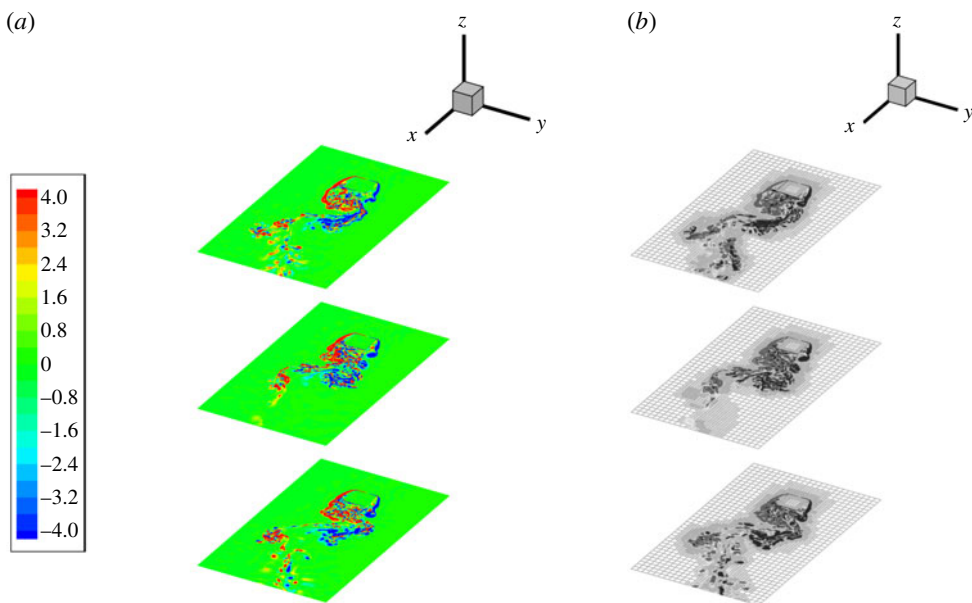


FIGURE 8. The adaptive LES solution at $Re = 2000$: spanwise vorticity contours ($-4 < \omega_z < 4$) (a) and computational mesh (b) in the planes $z = -1.2, 0$ and 1.2 , at a given time instant. Close-up view in the domain $-2 < x < 8, -3 < y < 3$.

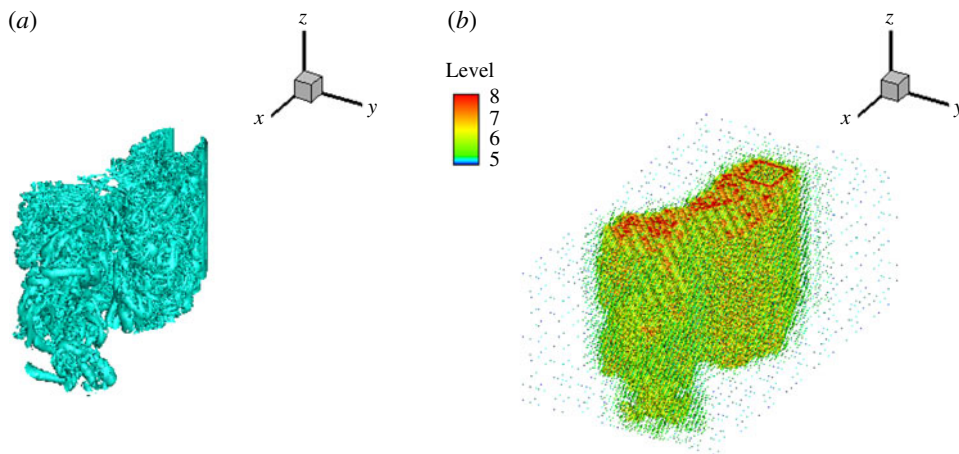


FIGURE 9. The adaptive LES solution at $Re = 2000$: main vortical structures in the near wake identified by the isosurfaces of $Q = 0.25$ (a) and scatter plot of the wavelet collocation points at higher levels of resolution ($5 \leq j \leq 8$) (b), at a given time instant. Close-up view in the domain $-2 < x < 8, -3 < y < 3$.

LDKM-G case and 8% in the LDKM-B case. Nevertheless, the two LES solutions are very similar and, for brevity, only the LDKM-G case will be considered in the following.

Similarly to the WDNS experiment, the adaptive LES solution is illustrated by examining the spanwise component of the vorticity field as well as the main vortical

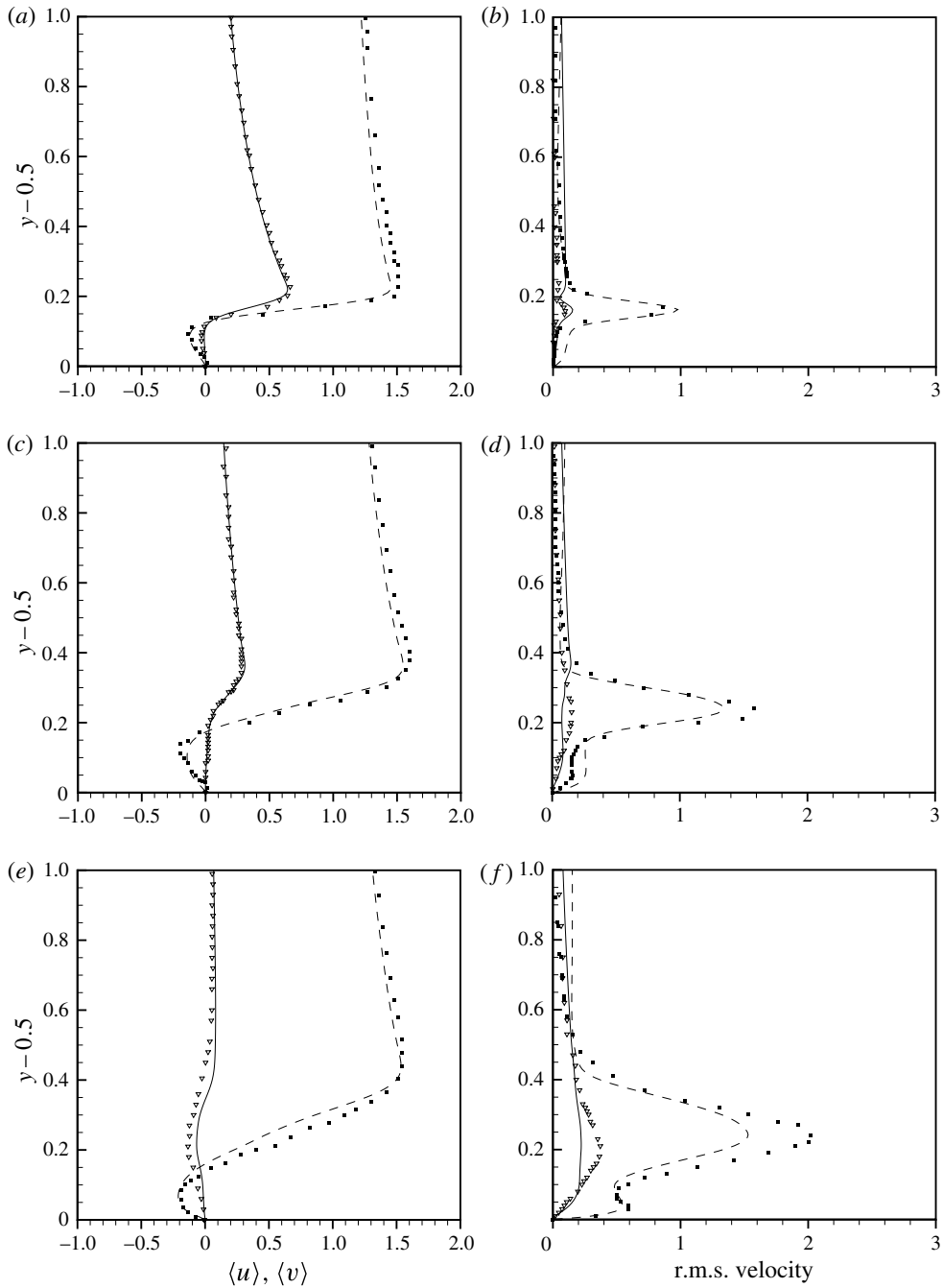


FIGURE 10. The adaptive LES solution at $Re = 2000$: mean (a,c,e) and r.m.s. (b,d,f) profiles of the streamwise (dashed line) and transverse (solid line) velocity components, at three different locations along the streamwise direction, $x = -0.3$ (a,b), 0 (c,d) and 0.3 (e,f), compared with reference data by Brun *et al.* (2008) (square and triangle symbols, respectively).

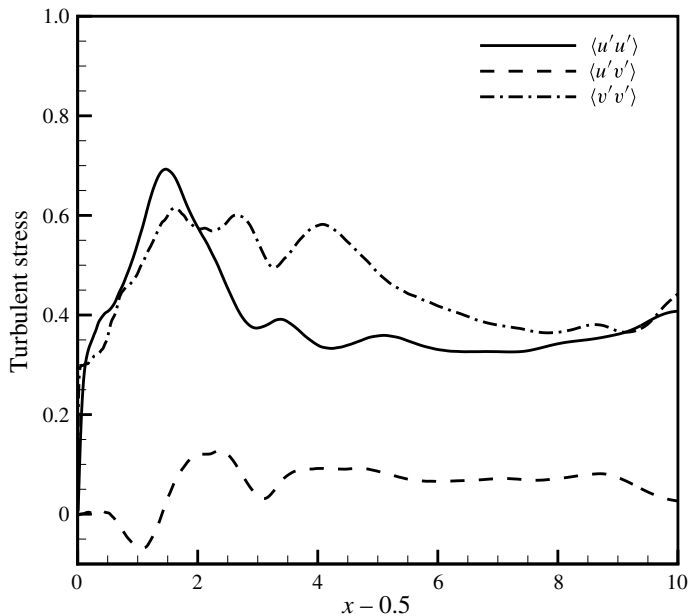


FIGURE 11. The adaptive LES solution at $Re = 2000$: profiles of the turbulent stresses along the wake centreline at $y = 0$.

structures in the near wake ($-2 < x < 8$). In figure 8, the contour maps of the instantaneous spanwise vorticity are depicted in three different planes ($z = -1.2, 0$ and 1.2) for the range $-4 < \omega_z < 4$ (a), together with the corresponding slices of the adaptive computational mesh (b). The main vortical structures, identified by the isosurfaces of $Q = 0.25$, are shown in figure 9(a). Panel (b) shows the related scatter plot of the collocation points associated with the retained wavelets, coloured by the variable grid level in the range $5 \leq j \leq 8$. The capacity of the present method to dynamically adapt to the flow evolution is confirmed. As is expected for this high supercritical Reynolds number, the separating shear layers on the sides of the cylinder are observed to become unstable and a transition to turbulent flow occurs (Lyn & Rodi 1994).

The present adaptive LES solution is validated against the one presented in Brun *et al.* (2008) by considering the profiles of the streamwise and transverse velocity components in the separated flow on the side of the cylinder for three different locations along the streamwise direction, namely $x = -0.3, 0$ and 0.3 . The mean streamwise and transverse velocities, say $\langle u \rangle$ and $\langle v \rangle$, are defined as the time- and spanwise-averaged corresponding components of the total velocity vector (perturbation velocity plus free stream velocity). By looking at figure 10(a,c,e), where the mean velocity profiles are drawn, it appears that the agreement with reference data is very good for each location. Some slight differences exist for the r.m.s. velocity profiles, which are reported in figure 10(b,d,f). However, the comparison seems fully satisfactory, even considering the different numerical settings like, for instance, the different blockage ratio, which affects the transition to turbulence in the separated shear layer.

The adaptive LES solution is further illustrated by examining the profiles along the wake centreline ($y = 0$) of the mean turbulent stresses $\langle u^2 \rangle$, $\langle u'v' \rangle$ and $\langle v^2 \rangle$, where

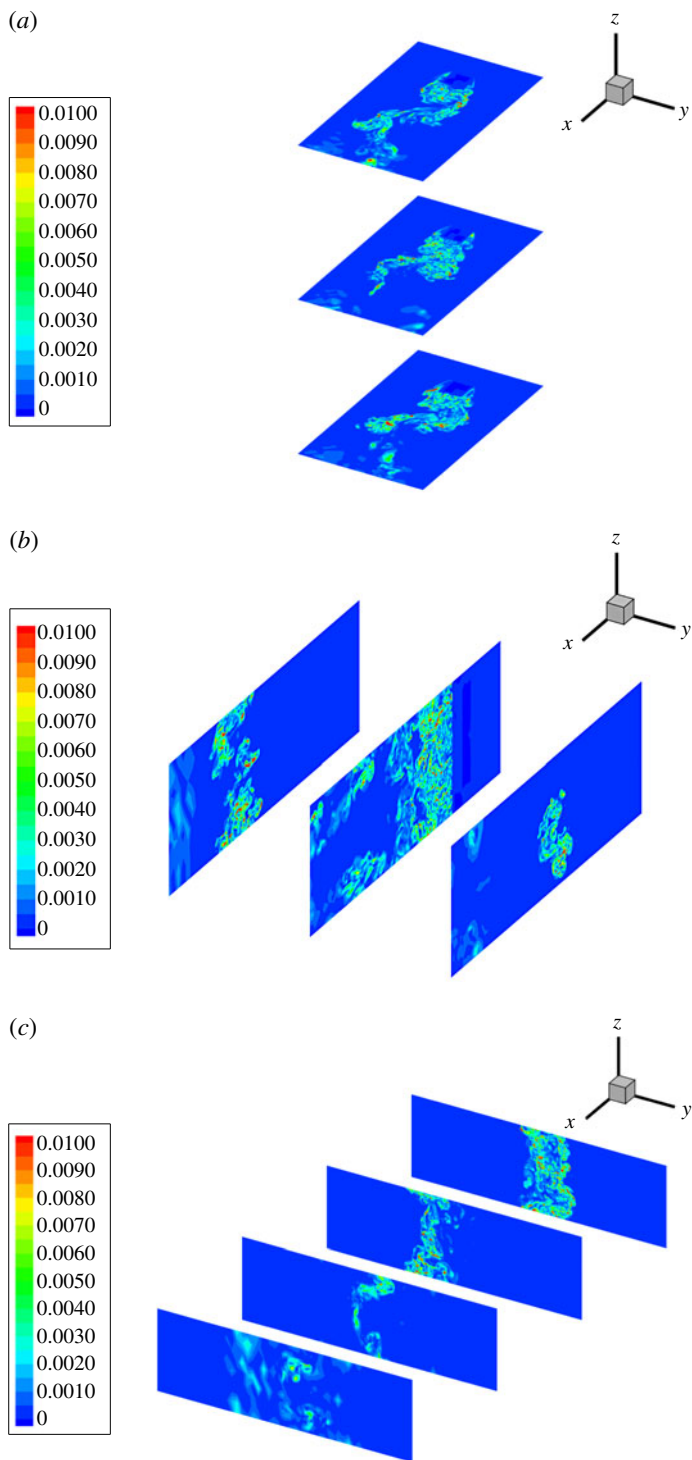


FIGURE 12. The adaptive LES solution at $Re = 2000$: instantaneous SGS energy contours ($0 < k_{sgs} < 0.01$) in the planes $z = -1.4, 0$ and 1.4 (a), $y = -1.5, 0$ and 1.5 (b) and $x = 2, 4, 6$ and 8 (c).

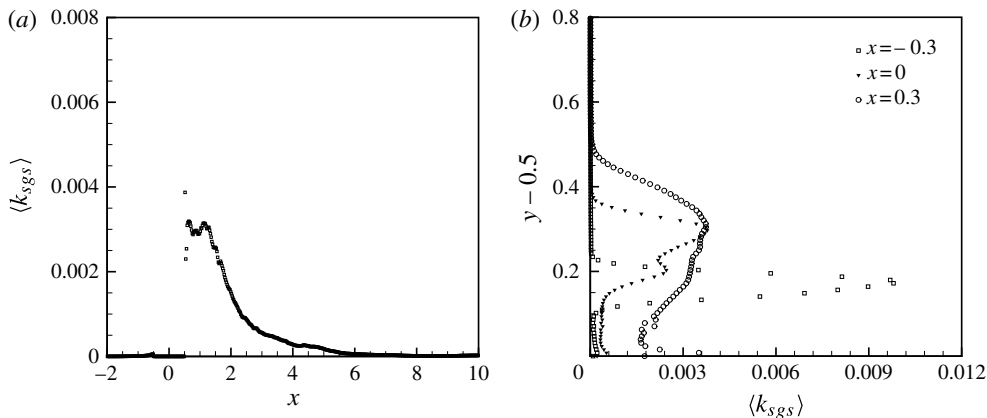


FIGURE 13. The adaptive LES solution at $Re = 2000$: profiles of the mean SGS energy $\langle k_{sgs} \rangle$ along the wake centreline at $y = 0$ (a) and on the side of the cylinder at $x = -0.3$, 0 and 0.3 (b).

u' and v' are the fluctuations around the corresponding means, reported in figure 11. The present method is able to predict the peak in the streamwise turbulent stress $\langle u'^2 \rangle$ that exists in the near wake of the cylinder, e.g. Lyn *et al.* (1995).

The contour maps of the SGS energy field are reported in figure 12 for the range $0 < k_{sgs} < 0.01$, at a given time instant. Three different sets of slices are drawn, which correspond to the planes $z = -1.4, 0$ and 1.4 (a), $y = -1.5, 0$ and 1.5 (b) and $x = 2, 4, 6$ and 8 (c). The level of SGS energy is relatively high in the near wake of the cylinder, while it vanishes inside the volume occupied by the obstacle, due to the penalization. This is also evident in figure 13, where the profiles of the mean SGS energy, $\langle k_{sgs} \rangle$, are represented along the wake centreline at $y = 0$ (a) and on the side of the cylinder at $x = -0.3, 0$ and 0.3 (b).

Finally, for the aerodynamic force arising from the fluid–structure interaction, the time-averaged drag coefficient is $\overline{C}_D = 2.2$ and the corresponding dominant wake frequency, calculated from the fluctuating lift force, results in a Strouhal number of $St = 0.13$. These results are in agreement with both experiments and numerical solutions at the same Reynolds number (Okajima 1982; Brun *et al.* 2008).

5. Concluding remarks

The hybrid volume-penalization/wavelet-collocation method for the simulation of unsteady three-dimensional incompressible flow around a square cylinder at zero incidence is studied. The computations have been conducted for both transitional flow, where the wake develops complex three-dimensional vortical structures, and turbulent flow, without and with the aid of a residual stress model. The present results are in general agreement with non-adaptive numerical solutions and experiments.

The advantages of combining these two numerical techniques for simulation of the fluid–structure interaction have been clearly demonstrated. At relatively low Reynolds number, the method allows the three-dimensional direct simulation of the shedding flow to be performed with a reasonable computational cost, while directly controlling the errors in the numerical approximation. On the other hand, at moderately high Reynolds number, the penalized wavelet-based adaptive LES method, supplied with

the LDKM, is able to reproduce the space–time evolution of the main flow structures. Since there is a one-to-one relationship between the level of wavelet thresholding and the degree of turbulence resolution, either one can be prescribed by the user in a practical calculation.

Due to its flexibility and efficiency, the proposed combined method appears to be very promising for the simulation of more challenging flows. For instance, higher Reynolds number and/or more complex geometry bluff body flows could be considered, where the adaptive wavelet-based methods are expected to become even more efficient.

Acknowledgements

This work was supported by the NSF under grant No. CBET-1236505. This support is gratefully acknowledged. The authors are also grateful for the computing time on the Janus supercomputer, which is supported by the National Science Foundation (award number CNS-0821794) and the University of Colorado Boulder. The Janus supercomputer is a joint effort of the University of Colorado Boulder, the University of Colorado Denver and the National Center for Atmospheric Research.

REFERENCES

- ANGOT, P., BRUNEAU, C. -H. & FABRIE, P. 1999 A penalization method to take into account obstacles in incompressible viscous flows. *Numer. Math.* **81**, 497–520.
- BRUN, C., AUBRUN, S., GOOSSENS, T. & RAVIER, PH. 2008 Coherent structures and their frequency signature in the separated shear layer on the sides of a square cylinder. *Flow Turbul. Combust.* **81**, 97–114.
- CARBOU, G. & FABRIE, P. 2003 Boundary layer for a penalization method for viscous incompressible flow. *Adv. Difference. Equ.* **8** (12), 1409–1532.
- DE STEFANO, G., DENARO, F. M. & RICCARDI, G. 1998 Analysis of 3D backward-facing step incompressible flows via a local average-based numerical procedure. *Intl J. Numer. Meth. Fluids* **28**, 1073–1091.
- DE STEFANO, G. & VASILYEV, O. V. 2010 Stochastic coherent adaptive large eddy simulation of forced isotropic turbulence. *J. Fluid Mech.* **646**, 453–470.
- DE STEFANO, G. & VASILYEV, O. V. 2012 A fully adaptive wavelet-based approach to homogeneous turbulence simulation. *J. Fluid Mech.* **695**, 149–172.
- DE STEFANO, G., VASILYEV, O. V. & GOLDSTEIN, D. E. 2008 Localized dynamic kinetic energy-based models for stochastic coherent adaptive large eddy simulation. *Phys. Fluids* **20** (4), 045102, 1–14.
- DUBIEF, Y. & DELCAYRE, F. 2000 On coherent-vortex identification in turbulence. *J. Turbul.* **1**, 1–22.
- FARGE, M., SCHNEIDER, K. & KEVLAHAN, N. 1999 Non-Gaussianity and coherent vortex simulation for two-dimensional turbulence using an adaptive orthogonal wavelet basis. *Phys. Fluids* **11** (8), 2187–2201.
- GOLDSTEIN, D. E. & VASILYEV, O. V. 2004 Stochastic coherent adaptive large eddy simulation method. *Phys. Fluids* **16** (7), 2497–2513.
- HUNT, J. C. R., WRAY, A. & MOIN, P. 1988 Eddies, stream, and convergence zones in turbulent flows. *Center for Turbulence Research Report*, CTR-S88.
- KEETELS, G. H., D'ORTONA, U., KRAMER, W., CLERCS, H. J. H., SCHNEIDER, K. & VAN HEIJST, G. J. F. 2007 Fourier spectral and wavelet solvers for the incompressible Navier–Stokes equations with volume-penalization: convergence of a dipole–wall collision. *J. Comput. Phys.* **227**, 919–945.
- KEVLAHAN, N. K.-R., ALAM, J. M. & VASILYEV, O. V. 2007 Scaling of space–time modes with Reynolds number in two-dimensional turbulence. *J. Fluid Mech.* **570**, 217–226.

- KEVLAHAN, N. K.-R. & VASILYEV, O. V. 2005 An adaptive wavelet collocation method for fluid–structure interaction at high Reynolds numbers. *SIAM J. Sci. Comput.* **26** (6), 1894–1915.
- LUO, S. C., CHEW, Y. T. & NG, Y. T. 2003 Characteristics of square cylinder wake transition flows. *Phys. Fluids* **15** (9), 2549–2559.
- LYN, D. A., EINAV, S., RODI, W. & PARK, J. H. 1995 A laser-Doppler velocimetry study of ensemble-averaged characteristics of the turbulent flow near wake of a square cylinder. *J. Fluid Mech.* **304**, 285–319.
- LYN, D. A. & RODI, W. 1994 The flapping shear layer formed by flow separation from the forward corner of a square cylinder. *J. Fluid Mech.* **267**, 353–376.
- NEJADMALAYERI, A. R. 2012 Hierarchical multiscale adaptive variable fidelity wavelet-based turbulence modeling with lagrangian spatially variable thresholding. PhD thesis, University of Colorado Boulder, Boulder, CO.
- NEJADMALAYERI, A., VEZOLAINEN, A. & VASILYEV, O. V. 2013 Reynolds number scaling of coherent vortex simulation and stochastic coherent adaptive large eddy simulation. *Phys. Fluids* **25**, 110823, 1–15; doi:10.1063/1.4825260.
- OKAJIMA, A. 1982 Strouhal numbers of rectangular cylinders. *J. Fluid Mech.* **123**, 379–398.
- ROBICHAUX, J., BALACHANDAR, S. & VANKA, S. P. 1999 Three-dimensional Floquet instability of the wake of square cylinder. *Phys. Fluids* **11**, 560–578.
- SAHA, A. K., BISWAS, G. & MURALIDHAR, K. 2003 Three-dimensional study of flow past a square cylinder at low Reynolds numbers. *Intl J. Heat Fluid Flow* **24**, 54–66.
- SAHA, A. K., MURALIDHAR, K. & BISWAS, G. 2000 Experimental study of flow past a square cylinder at high Reynolds numbers. *Exp. Fluids* **29**, 553–563.
- SCHNEIDER, K. & VASILYEV, O. V. 2010 Wavelet methods in computational fluid dynamics. *Annu. Rev. Fluid Mech.* **42**, 473–503.
- SHEARD, G. J., FITZGERALD, M. J. & RYAN, K. 2009 Cylinders with square cross-section: wake instabilities with incidence angle variation. *J. Fluid Mech.* **630**, 43–69.
- SOHANKAR, A., NORBERG, C. & DAVIDSON, L. 1999 Simulation of three-dimensional flow around a square cylinder at moderate Reynolds numbers. *Phys. Fluids* **11**, 288–306.
- VASILYEV, O. V. 2003 Solving multi-dimensional evolution problems with localized structures using second generation wavelets. *Intl J. Comput. Fluid Dyn.* **17** (2), 151–168; Special issue on High-Resolution Methods in Computational Fluid Dynamics.
- VASILYEV, O. V. & BOWMAN, C. 2000 Second generation wavelet collocation method for the solution of partial differential equations. *J. Comput. Phys.* **165**, 660–693.
- VASILYEV, O. V., DE STEFANO, G., GOLDSTEIN, D. E. & KEVLAHAN, N. K.-R. 2008 Lagrangian dynamic SGS model for stochastic coherent adaptive large eddy simulation. *J. Turbul.* **9** (11), 1–14.
- VASILYEV, O. V., LUND, T. S. & MOIN, P. 1998 A general class of commutative filters for LES in complex geometries. *J. Comput. Phys.* **146**, 105–123.
- WILLIAMSON, C. H. K. 1996 Vortex dynamics in the cylinder wake. *Annu. Rev. Fluid Mech.* **28**, 477–539.